Fermi surface electron-hole instability of the (TMTSF)$_2$PF$_6$ Bechgaard salt revealed by the first-principles Lindhard response function

Bogdan Guster[1]**, Miguel Pruneda**[1]**, Pablo Ordejón**[1]**, Enric Canadell**[2]**, Jean-Paul Pouget**[3]

[1]Catalan Institute of Nanoscience and Nanotechnology (ICN2), CSIC and The Barcelona Institute of Science and Technology, Campus Bellaterra, 08193 Barcelona, Spain
[2]Institut de Ciència de Materials de Barcelona (ICMAB-CSIC), Campus Bellaterra, 08193 Bellaterra, Spain
[3]Laboratoire de Physique des Solides, CNRS UMR 8502, Université de Paris-Sud, Universié Paris-Saclay, 91405 Orsay, France

Abstract. We report the first-principles DFT calculation of the electron-hole Lindhard response function of the (TMTSF)$_2$PF$_6$ Bechgaard salt using the real triclinic low-temperature structure. The Lindhard response is found to change considerably with temperature. Near the $2k_F$ spin density wave (SDW) instability it has the shape of a broad triangular plateau as a result of the multiple nesting associated with the warped quasi-one-dimensional Fermi surface. The evolution of the $2k_F$ broad maximum as well as the effect of pressure and deuteration is calculated and analyzed. The thermal dependence of the electron-hole coherence length deduced from these calculations compares very well with the experimental thermal evolution of the $2k_F$ Bond Order Wave correlation length. The existence of a triangular plateau of maxima in the low-temperature electron-hole Lindhard response of (TMTSF)$_2$PF$_6$ should favor a substantial mixing of q-dependent fluctuations which can have important consequences in understanding the phase diagram of the $2k_F$ SDW ground state, the mechanism of superconductivity and the magneto-transport of this paradigmatic quasi-one-dimensional material. The first-principles DFT Lindhard response provides a very accurate and unbiased approach to the low-temperature instabilities of (TMTSF)$_2$PF$_6$ which can take into account in a simple way 3D effects and subtle structural variations, thus providing a very valuable tool in understanding the remarkable physics of molecular conductors.

1. Introduction

At the simplest level of description the electronic properties of quasi-one dimensional (1D) conductors are governed by two antagonist interactions: inter-chain transfer integrals ($t_\perp$) and inter-site Coulomb repulsions (V_{ij}). The former tend to delocalize carriers on neighboring chains leading to the formation of 2D or 3D anisotropic metals. In contrast, the latter tend to localize the carriers on individual chains leading to the formation of 1D Luttinger liquids [1]. The pertinence of this basic approach is illustrated by the isostructural series of quarter-filled Fabre (TMTTF)$_2$X and Bechgaard (TMTSF)$_2$X organic salts where TMTTF is tetramethyltetrathiafulvalene, TMTSF is tetramethyltetraselenafulvalene and X is a monovalent anion which in the present work is PF$_6^-$. The structure of (TMTSF)$_2$PF$_6$ is shown in Fig. 1 [2] where slightly dimerized zig-zag stacks of TMTSF donor molecules run along the a direction. The organic stacks form (a,b) layers which delimit cavities along c* which are filled with monovalent (X$^-$) anions. The temperature-pressure (T-P) phase diagram of Fabre and Bechgaard salts incorporating centrosymmetric anions such as PF$_6$ (see Fig. 2) shows that 1D hole localization in the donor stacks dominates in the (TMTTF)$_2$PF$_6$ Fabre salt at ambient pressure, while the intra-stack metallic hole delocalization is the relevant aspect for the (TMTSF)$_2$PF$_6$ Bechgaard salt [3]. The generalized phase diagram of Fig. 2 is also controlled by pressure since the inter-stack transfer integrals, $t_\perp$, are enhanced under applied pressure. [4, 5, 6].

Earlier studies [7, 8] clearly pointed out the difference between the inter-chain diffusive electron transfer and coherent electron transfer mechanisms. In the first case there is no coherence between Bloch functions located on neighbouring chains. Thus, in that case one has a true 1D metal where the warping of the Fermi surface (FS) is not relevant and there is no transverse plasma edge. In the second case, the electronic wave function is 2D or 3D, delocalized over several chains, and $t_\perp$ is a relevant interaction. More precisely, for a non-interacting electron gas the coherent regime occurs for k_BT< $t_\perp/\pi = k_B$T$_{CO}$, where T$_{CO}$ is the 1D to 2D/3D crossover temperature [8, 9] and below T$_{CO}$ a transverse plasma edge should be detected. It has been predicted [10, 11] that the crossover transition T$_{CO}$

between the diffusive and coherent regimes decreases in the presence of sizeable intra-chain Coulomb repulsions because the latter tend to localize the electron wave packets so that the effective inter-chain tunneling process should be reduced. This leads to a downward renormalized T$_{CO}$, at which temperature there is a deconfinement transition from a 1D Luttinger liquid to a 2D or 3D Fermi liquid [12]. However, beyond this qualitative picture, there are many important theoretical questions which should be elucidated in order to quantitatively describe the deconfinement transition [1]. These considerations should particularly apply to quasi-1D organic metals. In (TMTSF)$_2$PF$_6$, for instance, the 1D to 2D deconfinement temperature T$_{CO}$ at ambient pressure is found to occur at $\sim$ 100 K on the basis of the detection of a transverse plasma edge when an electric field is applied along b [6] as well as from the change of slope of the c* transverse electrical conductivity [13]. As shown in Fig. 2, T$_{CO}$ substantially increases under pressure. In contrast with (TMTSF)$_2$PF$_6$, which exhibits intra-stack metallic conductivity, a charge localization occurs in (TMTTF)$_2$PF$_6$ below T$_\rho \sim$ 230 K at ambient pressure, as proved by the occurrence of an activated intra-stack conductivity [14]. Due to this fact T$_{CO}$ is renormalized to 0 K [3]. When pressurized, T$_\rho$ for (TMTTF)$_2$PF$_6$ decreases (Fig. 2) and the behavior typical of the Bechgaard salts is recovered [3].

According to the present DFT calculations the transfer integrals for (TMTSF)$_2$PF$_6$ at 300 K along the a, b and c* directions are $t_a \approx$ 210 meV, $t_b^{eff} \approx$ 28 meV and $t_{c^*} \approx$ 0.8 meV, respectively (t_b^{eff} is the effective transfer integral along b according to the tight-binding model of Yamaji [15, 16]). As expected from the crystal structure (Fig. 1), these values imply a highly anisotropic system. However, these transfer integrals are rather similar to those calculated for (TMTTF)$_2$PF$_6$ under the same conditions: $t_a \approx$ 180 meV, $t_b^{eff} \approx$ 24 meV and t_c*$\approx$ 0.5 meV at 300 K. Thus, the differences in the phase diagram between the Bechgaard and Fabre salts should be attributed to the presence of stronger Coulomb repulsions in the TMTTF vs. TMTSF stacks. Such difference is clearly evidenced by the observation of $4k_F$ Wigner-type charge density wave (CDW) instabilities in salts with uniform TMTTF stacks but $2k_F$ Peierls-type CDW instabilities in salts with uniform TMTSF stacks (k_F is the Fermi wave vector of the donor
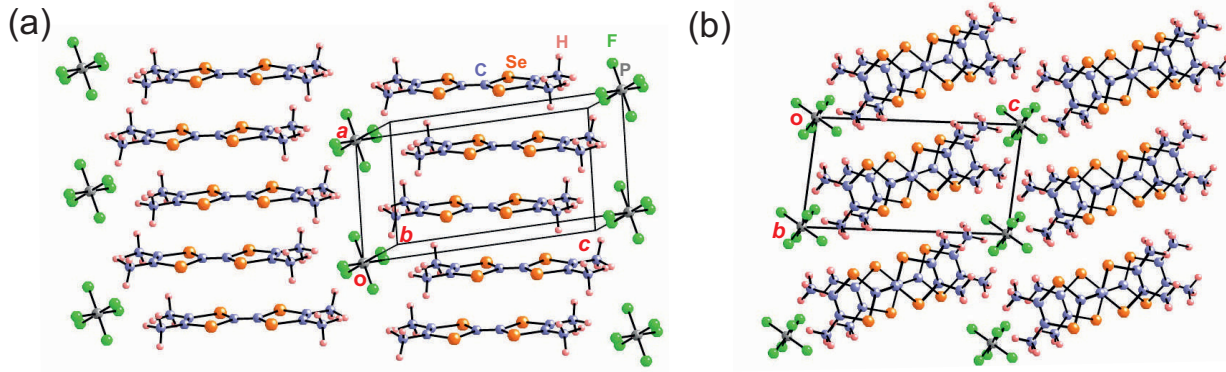
Figure 1. Crystal structure of the $(TMTSF)_2PF_6$ Bechgaard salt: (a) Quasi-planar organic molecules stack along the a axis and are separated along the c^* direction by PF_6^- anions. (b) Projection of the $(TMTSF)_2PF_6$ structure along the stack direction.
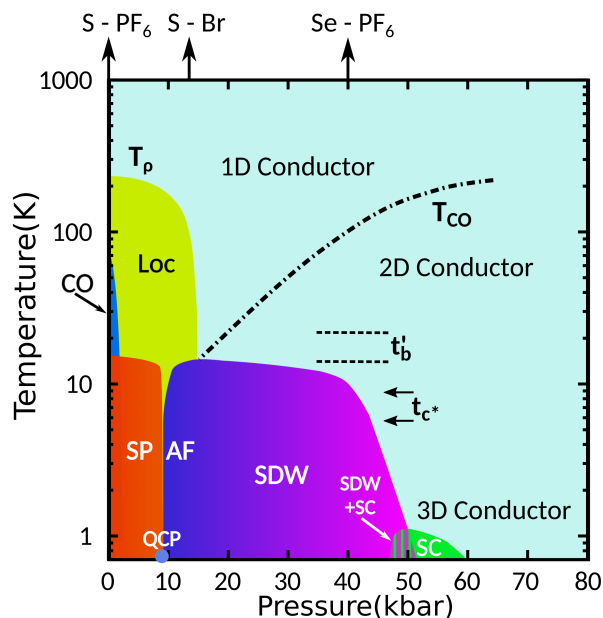

Figure 2. Generalized phase diagram for the Fabre (S-X) and Bechgaard (Se-X) salts where X is a centrosymmetric anion. The pressure scale corresponds to $(TMTTF)_2PF_6$. Vertical arrows place $(TMTTF)_2Br$ and $(TMTSF)_2PF_6$ at atmospheric pressure in the phase diagram. CO, SP, AF, SDW and SC refer to charge ordered, Spin-Peierls, antiferromagnetic, spin density wave and superconducting ground states. QCP is a quantum critical point between the SP and AF ground states. T_ρ indicates the onset temperature for charge localization (Loc in the Figure) as detected in the conductivity measurements. T_{CO} is the crossover temperature from a 1D (in the stack direction (a) to a 2D (in the (a,b) donor layer) delocalized electron gas according to ref [6]. On the right hand scale there is also a crossover to a 3D delocalization regime along c^* through the anion cavities at a temperature of the order of t_{c^*}. The value of the nesting breaking term t'_b introduced in the text is also indicated.

stacks 1D electron gas) [17]. The strong intra-stack Coulomb repulsions in the 1D electronic regime of $(TMTTF)_2PF_6$ at high temperature lead to a $4k_F$ hole localisation on the bonds of the donor zig-zag chains. Note that the charge localization on the donor dimers of the Fabre salts can be viewed as being stabilized by the response of the $4k_F$ CDW instability of the TMTTF stacks to the $4k_F$ potential set by the anion sublattice [18, 19, 20]. Charge localization induces a spin-charge decoupling so that the spin degrees of freedom drive anti-ferromagnetic (AF) or spin-Peierls (SP) low-temperature orders in the Fabre salts as shown in Fig. 2.

In contrast, $(TMTSF)_2PF_6$ is a room temperature metallic conductor whose electronic dimensionality changes from 1D to 2D at $T_{CO} \sim 100$ K at ambient pressure. Thus, below T_{CO} the warping along b^* of the open sheets at $\pm k_F = \pm a^*/2$ FS should be thermally relevant. In this context, it was suggested [16] that a $2k_F$ FS nesting process could be responsible for the stabilization of the $2k_F$ spin density wave (SDW) insulating ground state detected below $T_{SDW} = 12$ K at ambient pressure. This mechanism was sustained by the NMR measurement of a SDW modulation component of 0.20-$0.24b^*$ [21, 22] which agrees with the best nesting wave vector [23] of a FS modeled according to the tight-binding *pseudo-orthorhombic approximation* of Yamaji [15, 16]. After this agreement was noticed, FS nesting effects became the key ingredient to elucidate the low-temperature (low-energy) physics of the Bechgaard salts. In particular, a significant decrease of T_{SDW} was observed under pressure (Fig. 2) and, when the metallic state is restored above ~ 9.5 kbar, $(TMTSF)_2PF_6$ becomes superconducting at $T_S \approx 1.2$ K [24]. This effect is ascribed to the suppression of the FS nesting when pressure enhances the magnitude of the so-called FS nesting breaking or (unnesting) term along b^* (t'_b, estimated to be 14-22 K at ambient pressure in

the *pseudo-orthorhombic approximation*, see below in Sect. 3 and Fig. 2). The drastic effect of the t'_b on the SDW phase diagram was quantitatively analyzed using an *orthorhomic approximation* of the electronic structure of Bechgaard salts [15, 16, 25, 26]. Note also that when the low-temperature metallic state is restored and when the inter-layer transport becomes coherent, a 2D to 3D electronic crossover is expected. The detection of a weak transverse Drude edge below 10 K in metallic $(TMTSF)_2ClO_4$ Bechgaard salt at ambient pressure [27] corroborates that the 3D electronic crossover temperature is of the order of t_{c*} and occurs above the superconducting transition.

Remarkably, in the 3D metallic state when superconductivity vanishes under a high magnetic field, a cascade of induced SDW ground states has been detected when the applied magnetic field along $c*$ exceeds a threshold related to the FS nesting breaking term along this direction, t'_c. These field induced SDW phases (FISDW) are due to the quantization of the 2D orbital movement in pockets remaining because of the imperfect FS nesting along $b*$. Thus, the occurrence of FS nesting breaking terms is needed to account for the occurrence of FISDW phases. A quantitative analysis of the FISDW instability has been performed from the calculation of the Lindhard function in the presence of a magnetic field within the *orthorhomic approximation* of the electronic structure [16, 28, 29, 30]. However the interpretation of additional observations, such as the reversal of sign of the quantum Hall effect between different FISDW phases, requires the existence of additional FS nesting breaking terms which were introduced in an *ad hoc* manner in the calculation of the Lindhard function [31] and whose origin needs to go beyond the *orthorhombic approximation*.

In summary, although FS nesting effects are the key ingredient to elucidate the low-temperature/low-energy physics of the Bechgaard salts, this quantitative analysis has been performed using an *orthorhombic* or *pseudo-orthorhombic* model of the electronic structure because of the difficulty to handle analytic calculations within the real triclinic structure of these salts. Present-day density functional theory (DFT)-based approaches are reliable enough to explore many aspects of the electronic structure of molecular conductors [32, 33, 34, 35]. Thus, here we revisit the FS nesting mechanism using an unbiased DFT approach and the real triclinic 3D crystal structure of the Bechgaard salt $(TMTSF)_2PF_6$. However as it is not easy to clearly appreciate nesting effects from the simple visual inspection of the FS we calculate and analyze the first-principles 3D electron-hole response function of this paradigmatic low-dimensional material and study in detail its temperature and wave vector dependence.

2. Computational details

The DFT calculations [36, 37] were carried out using a numerical atomic orbitals approach, which was developed for efficient calculations in large systems and implemented in the SIESTA code [38, 39]. We have used the generalized gradient approximation (GGA) to DFT and, in particular, the functional of Perdew, Burke and Ernzerhof [40]. Only the valence electrons are considered in the calculation, with the core being replaced by norm-conserving scalar relativistic pseudopotentials [41] factorized in the Kleinman-Bylander form [42]. The non-linear core-valence exchange-correlation scheme [43] was used for all elements. We have used a split-valence double-ζ basis set including polarization functions [44]. The energy cutoff of the real space integration mesh was 350 Ry. The Brillouin zone (BZ) was sampled with the Monkhorst-Pack scheme [45] using grids of $(45\times45\times18)$ k-points to build the charge density. The Lindhard response function,

$$\chi(q) = -\sum_{i,j} \sum_k \frac{f_F(\epsilon_i(k)) - f_F(\epsilon_j(k+q))}{\epsilon_i(k) - \epsilon_j(k+q)}, \qquad (1)$$

where f_F is the Fermi function and $\epsilon_i(k)$ are the band eigenvalues, was obtained from the computed DFT band eigenvalues $\epsilon_i(k)$ (i.e. in this work the TMTSF HOMO-based bands of the system). The integral over k-points of the BZ was approximated by a direct summation over a dense, regular grid of points. As the Lindhard function is more sensitive to the accuracy of the BZ integration than the total energy, especially in very anisotropic systems, and/or in the presence of hot spots in the band structure (e.g. saddle points with the corresponding van Hove singularity in the DOS), the k-points grid used for its calculation must be more dense than in the standard self-consistent determination of the charge density and Kohn-Sham energy. The calculations are done, nevertheless, using the eigenvalues obtained in the DFT calculation for the coarser grid, and interpolating their values in the denser grid, using a post-processing utility available within the SIESTA package. In this work, for the calculation of the Lindhard response function, the BZ was sampled using a grid of $(400\times400\times16)$ k-points. The partially filled bands were those taken into account in the calculations. The DFT calculations reported here have been performed using three different crystal structures: (i) protonated $(TMTSF)_2PF_6$-H_{12} at 4 K [46] and ambient pressure, (ii) protonated $(TMTSF)_2PF_6$-H_{12} at 1.7 K and 7 kbar [47], and (iii) 98 % deuterated $(TMTSF)_2PF_6$-D_{12} at 4 K and ambient pressure [48]. Note that the thermal dependences of the Lindhard functions reported below are due to the Fermi function in Eq. 1.
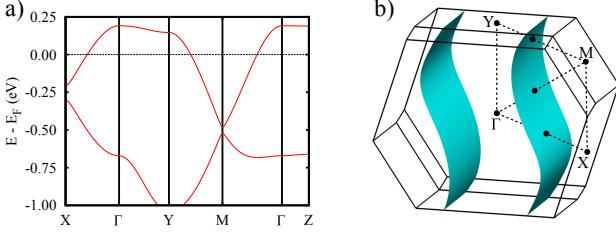
3. Electronic Structure

Figure 3. Calculated band structure (a) and Fermi surface (b) for $(TMTSF)_2PF_6$ using the 4 K crystal structure. The energy zero corresponds to the Fermi level. $\Gamma = (0, 0, 0)$, X = (1/2, 0, 0), Y = (0, 1/2, 0), Z = (0, 0, 1/2) and M = (1/2, 1/2, 0) in units of the triclinic reciprocal lattice vectors.

The calculated band structure near the Fermi level for the 4 K crystal structure of $(TMTSF)_2PF_6$ is shown in Fig. 3a. The two bands are almost exclusively built from the HOMO of TMTSF and because of the stoichiometry they contain one hole so that the upper band is half-filled. The total dispersion of these bands is 1.23 eV and the dimerization gap at X is 96 meV. The two bands exhibit quite different dispersion along the b^* inter-chain direction, the upper one being considerably flatter. These features agree with other reported band structures [49, 23, 5, 50]. Fitting the DFT results to the tight-binding model of Yamaji [15, 16] leads to the following values of the transfer integrals along the a, b and c^* directions for the PF_6 salt at 4 K: $t_a \approx 256$ meV, $t_b^{eff} \approx 38$ meV and $t_{c^*} \approx 0.5$ meV, respectively. Thermal contraction from 300 K to 4 K leads to increases of 23% and 33 % for t_a and t_b^{eff} and a decrease of 37% for t_{c^*}, respectively. In the same temperature range the variation is considerably smaller for the isostructural $(TMTTF)_2PF_6$ Fabre salt: 13% and 11% increase for t_a and t_b^{eff}, respectively, and 5% decrease for t_{c^*}. Another interesting quantity is the so-called nesting breaking (or unnesting) parameter [16, 15, 26] mentioned above,

$$t'_b = \frac{1}{2\sqrt{2}} \frac{t_b^2}{t_a} \qquad (2)$$

which measures how much the actual FS differs from the perfect nesting condition within Yamaji's tight-binding model. Using the above transfer integrals t'_b for $(TMTSF)_2PF_6$ is estimated to be -1.9 meV (21.7 K) (see Fig. 2).

Drude analysis of infrared measurements for $(TMTSF)_2PF_6$ leads to $t_a \approx 0.25$ eV and $t_{b'} \approx 22$ meV (at 30 K) (b' is the intra-layer transverse direction perpendicular to a) [51]. t_a is in excellent agreement with our calculated value, 0.256 eV. $t_{b'}$ is slightly smaller than our t_b^{eff} value. Note however that the measurement of the conductivity anisotropy
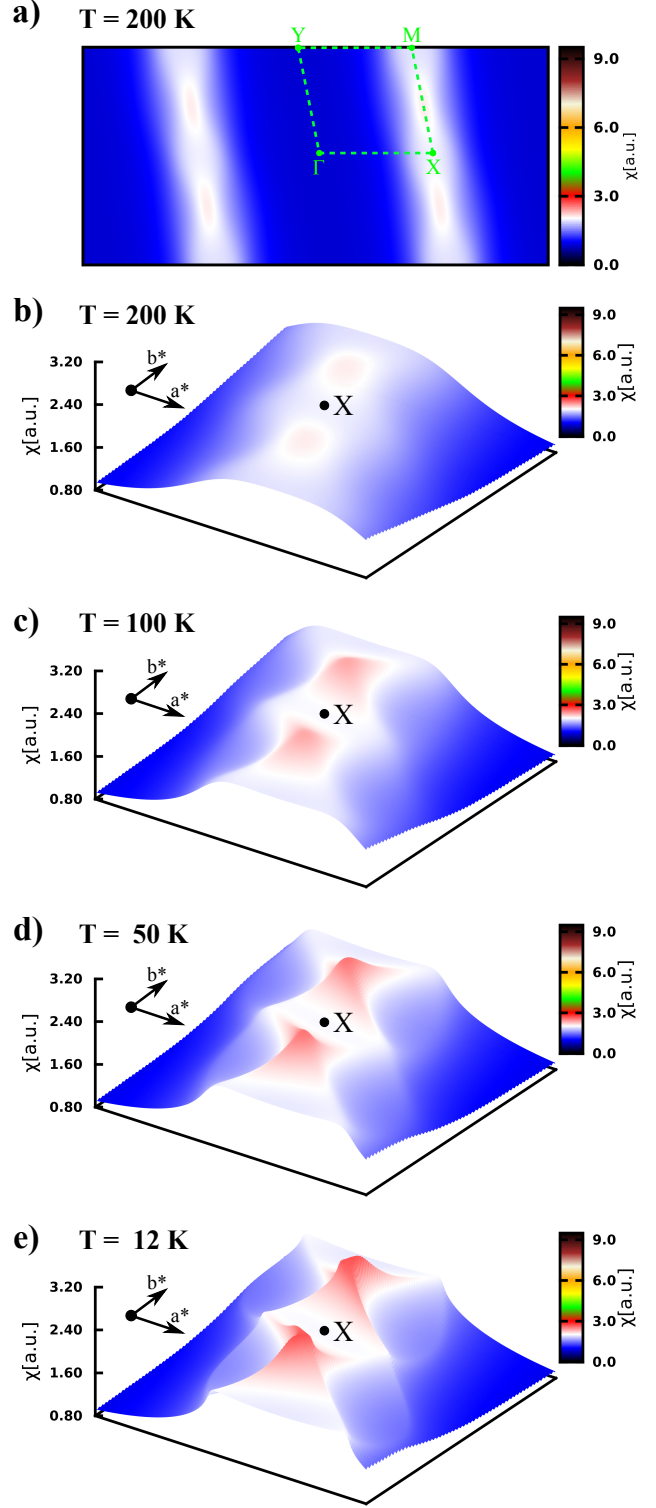

Figure 4. 2D (a) and 3D (b) plots of the Lindhard function of $(TMTSF)_2PF_6$ in the (a^*, b^*) reciprocal plane at 200 K. (c)-(e) 3D plots at 100 K, 50 K and $T_{SDW} = 12$ K, respectively.
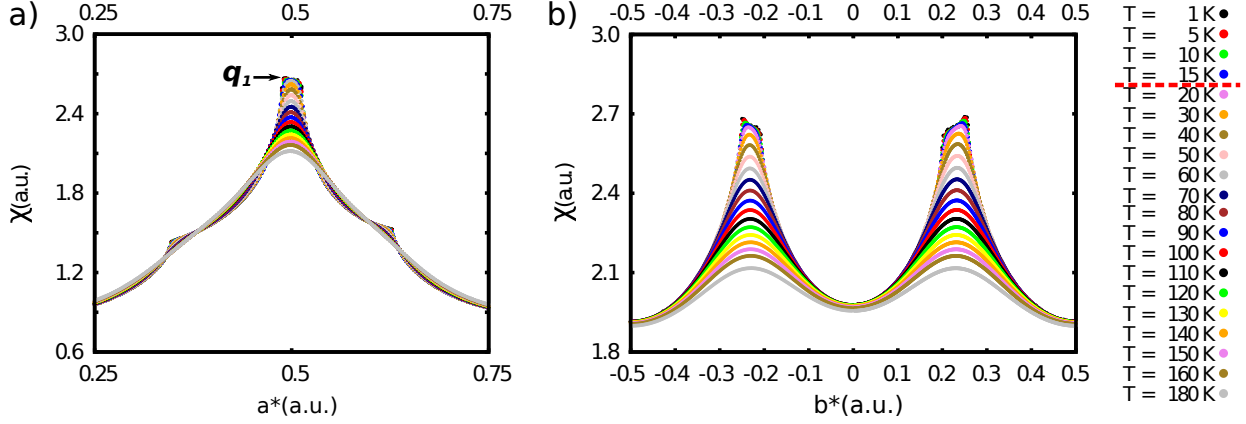
Figure 5. Thermal dependence of the: (a) longitudinal a^* scans across the Lindhard function of $(TMTSF)_2PF_6$ at 0.23 b^* [i.e. $(xa^*, 0.23b^*)$ scans] and (b) transverse b^* scans at $0.5a^*$ [i.e. $(0.5a^*, xb^*)$ scans]. The red dashed line in the temperature scale indicates the temperature at which the single maximum leads to a tilted segment of maxima in (b). In part (a) the two kinks observed at $0.35a^*$ and $0.63a^*$ correspond to the crossing of the singularity lines mentioned in the text which separate the light blue and the dark blue regions in Fig. 8b.

in the SDW phase of $(TMTSF)_2PF_6$ leads to $t_{b'} \sim$ 35-28 meV [52] which is close to t_b^{eff}. Finally, the work of Zamborszky et al. [52] led to $t_{c^*} \approx 0.8$ meV which is comparable to our $t_{c^*} \approx 0.5$ meV value. Using an average of the first-principles t_b^{eff} values for 300 K and 4 K (33 meV), one estimates a 1D-2D deconfinement temperature for non-interacting electrons ($k_B T_{CO} = t_b^{eff}/k_B\pi$) of 90 K, which is close to the experimental determination of 100 K [6, 13]. Finally, the energy $4t_b'$ of remaining pockets due to nesting breaking effects in the SDW phase can be obtained from the difference between the direct SDW gap from optical measurements ($2\Delta = 100$ K) [53] and twice the activation gap of the conductivity ($2\Delta_{th} = 41$ K [52]-48 K [54]). From this difference one obtains $t_b' \approx$ 14 K, which is not far from the 21.7 K value estimated from Eq. 2.

The reasonable agreement between calculated and experimentally estimated transfer integrals shows that DFT calculations provide reliable electronic structure parameters for $(TMTSF)_2PF_6$ so that the Lindhard function calculations for this salt should be meaningful. The calculated FS for $(TMTSF)_2PF_6$ at 4 K is shown in Fig. 3b. In the absence of anion ordering transitions the shape of this FS is common to all Bechgaard salts with the only difference of slight variations in their warping. However these subtle differences are at the heart of their different low-temperature physics and the calculation of the 3D Lindhard function (see Sect. 4) is the best quantitative approach to understand it.

4. Analysis of the Lindhard function of $(TMTSF)_2PF_6$

In this section we will explore the temperature and wave vector dependencies of the first-principles
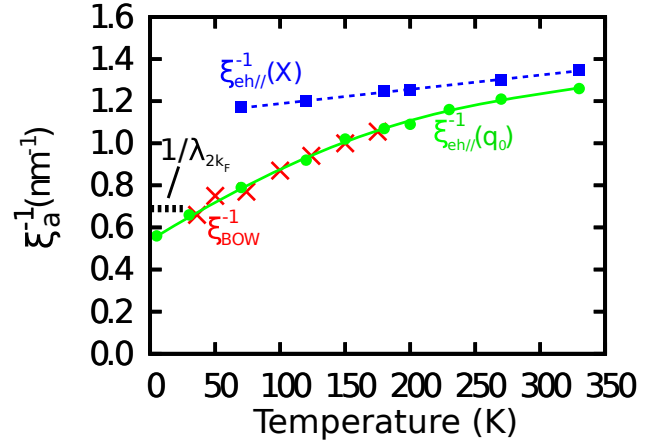

Figure 6. Comparison of the thermal dependence of the inverse electron-hole coherence length $\xi_{eh\|}^{-1}$ calculated at the q_0 and X points with the inverse BOW correlation length ξ_{BOW}^{-1} of $(TMTSF)_2PF_6$ measured in ref. [55].

Lindhard function for $(TMTSF)_2PF_6$ and later (Sect. 5) these results will be compared with those based on the *orthorhombic* or *pseudo orthorhombic approximation* as well as with the experimental information. Shown in Fig. 4 are intensity plots of the Lindhard function at 200 K (a) and (b), 100 K(c), 50 K(d) and $T_{SDW} = 12$ K (e) in the (a^*, b^*) reciprocal plane. As shown in these plots the response is very anisotropic. In addition, we have verified that the response does not vary with the inter-layer c^* wave vector component (this is not the case in other Bechgaard salts like the ClO_4 and NO_3 salts. [56]). At 200 K (Fig. 4a) the intensity of the response, which varies significantly along the a^* direction (see also the a^* scans in Fig. 5a) is centered around $q_{1D} = 0.5a^*$. This chain component amounts to the $2k_F$ wave
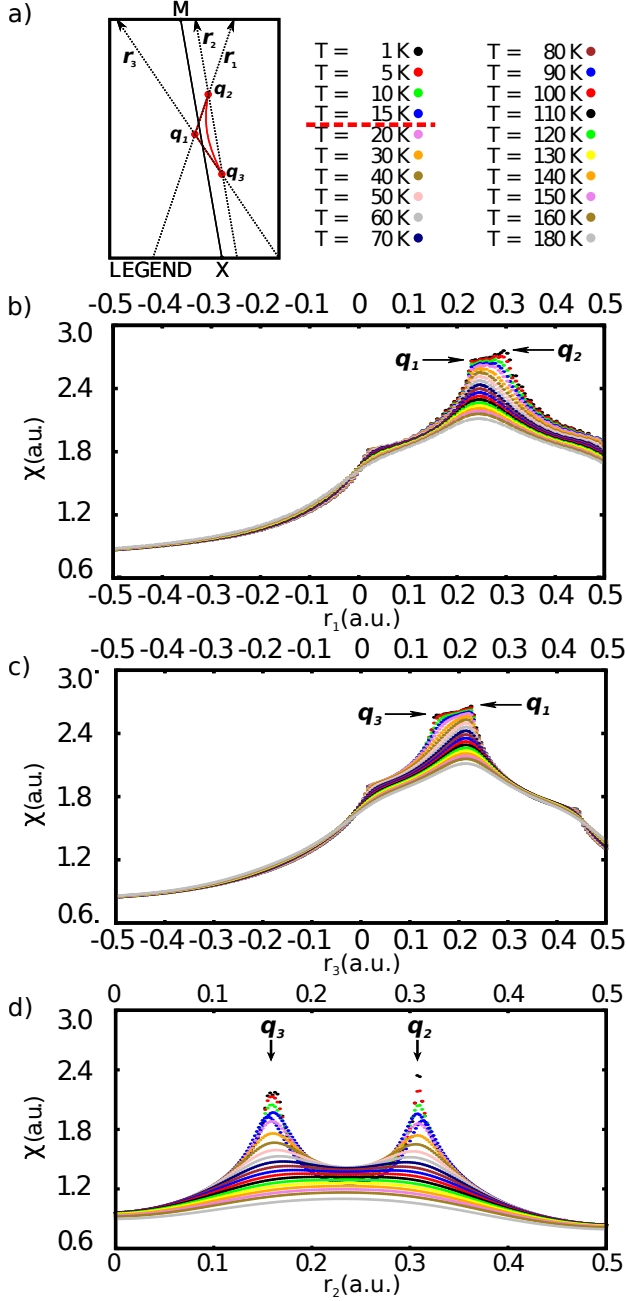
Figure 7. Thermal dependence of the scans across q_1-q_2 (b), q_3-q_1 (c) and q_2-q_3 (d) lines of the Lindhard function for $(TMTSF)_2PF_6$. In (a) we present a legend for the scans directions where $\vec{r}_1 = (1 - \tan(|\vec{q}_1 - \vec{q}_2|))a^* + b^*$, $\vec{r}_2 = -(1 + \tan(|\vec{q}_3 - \vec{q}_2|))a^* + b^*$ and $\vec{r}_3 = -(1 + \tan(|\vec{q}_3 - \vec{q}_1|))a^* + b^*$. Positive values are designated for q points above the Γ-X direction. Note the tilted plateau which continuously develops upon cooling in (b) and (c). The red dashed line in the temperature scale indicates the temperature at which the single maximum leads to a tilted segment of maxima. The kinks observed for q_1-$q_2 \sim 0$ and q_3-$q_1 \sim 0$ and 0.4 correspond to the crossing of singularity lines mentioned in the text which separate the light blue to dark blue regions in Fig. 8b.

number of the quasi-1D electron gas in a dimerized quarter-filled (hole) band structure. Fig. 4a shows that the 200 K response is slightly modulated along the b^* direction. The magnification along b^* in Fig. 4b reveals the presence of two broad maxima at about $\pm\,0.23b^*$ which are more clearly visualized on the b^* scans of Fig. 5b.

Upon cooling down to 100 K (Fig. 4c) there is a net increase in the intensity maxima of the Lindhard response. Figs. 5a and b show that the intensity increase concentrates around a broad maximum in $\pm q_0 = (0.5, \pm 0.23)$. In addition, when T decreases the global shape of the Lindhard response becomes sinusoidally modulated along a^* (Fig. 4c). As a consequence, the response along a^* remains broader at the X (0.5, 0) and M points (0.5, 0.5) and sharpens in-between these points near q_0. This is quantitatively illustrated by Fig. 6 giving the thermal dependence of the half-width at half-maximum (HWHM) of the response function along a^* at the X and q_0 points. This quantity corresponds to the inverse electron-hole coherence length in the chains direction ($1/\xi_{eh}$) which will be discussed and confronted with the experimental information in Sect. 5. Upon cooling $1/\xi_{eh}(X)$ stays roughly constant while $1/\xi_{eh}(q_0)$ gently decreases but does not vanish at low temperature. Finally, note also that the HWHM of the q dependence of the Lindhard function along b^* (Fig. 5b) leads to an inverse electron-hole inter-stack transverse coherence length of about 0.12-0.09 Å^{-1} between 200 K and 100 K. The inverse of this quantity, which is nearly constant when varying the temperature, is of the order of the inter-stack distance b. This means that, since the electron-hole pairs remain basically confined on the stack, it can be reasonably considered that *the high-temperature electron-hole response is essentially 1D. However, this picture must be modified below 100 K* because the shape of the Lindhard function drastically changes.

Fig. 4d shows a 3D plot of the intensity of the Lindhard function at 50 K. The asymmetric development of arcs of intensity can be clearly distinguished. More precisely, the maximum of the electron-hole response adopts a boomerang-like shape limited by the $q_1 \sim q_0$, q_2 and q_3 wave vectors whose components, schematically represented in Fig. 7a, will be carefully scrutinized below. The change of shape of the Lindhard response is illustrated by the diagonal q_1-q_2 and q_1-q_3 scans crossing q_{1D} shown in Figs. 7b and c, respectively. It can be clearly seen the progressive growth of intensity singularities at q_2 and q_3, away from $0.5a^*$, which upon cooling give rise to a continuum of intensity maxima transforming at low-temperature into a tilted segment joining q_1. The q_2-q_3 scans (Fig. 7d), which are out of the q_{1D} direction, clearly illustrate the progressive development of the q_2 and q_3
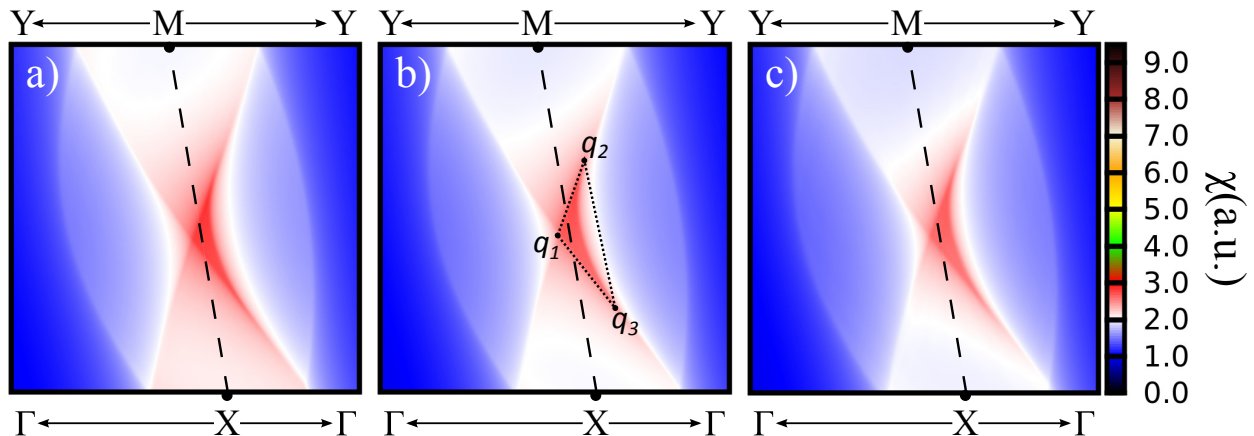
Figure 8. Magnified section of the Lindhard functions at 5 K for 98% deuterated $(TMTSF)_2PF_6-D_{12}$ at P_{atm} (a), protonated $(TMTSF)_2PF_6-H_{12}$ at P_{atm} (b), and protonated $(TMTSF)_2PF_6-H_{12}$ at 7 kbar pressure (c). The $X \rightarrow \Gamma$ and $M \rightarrow Y$ arrows are only used to indicate the associate directions. In (b) the q_1, q_2 and q_3 points used in the text are labelled.

maxima which limit the arc of intensity depicted in Fig. 7a. These maxima begin to be detected below 100 K (Fig. 7d). Upon further cooling the q_2 and q_3 maxima transform into singularities at $q_2 = (0.52, 0.30)$ and $q_3 = (0.53, 0.14)$ reciprocal positions. As a result, *a tilted plateau of intensity maxima develops around 15-20 K* and the Lindhard function exhibits well defined singularities at the q_0, q_2 and q_3 wave vector positions when the SDW transition occurs ($T_{SDW} = 12$ K, see Fig. 4d). At T_{SDW} the maximum of the Lindhard response occurs at the q_0 wave vector. However around 10 K the q_0 maximum shifts to $q_1 = (0.48, 0.23)$ (Fig. 5a) and the absolute maximum of intensity of the Lindhard response shifts to q_2 (see Figs. 7b).

Fig. 8b represents the curved and tilted triangular plateau of maxima of the Lindhard response delimited by the q_1, q_2 and q_3 wave vectors in protonated $(TMTSF)_2PF_6-H_{12}$ at 5 K and ambient pressure. This is compared with the 5 K Lindhard function calculated under the same conditions for deuterated $(TMTSF)_2PF_6-D_{12}$ (Fig. 8a) and protonated $(TMTSF)_2PF_6-H_{12}$ at 7 kbar (Fig. 8c) [47] respectively. The main differences between these Lindhard functions (see also Fig. 9 where we directly plot the differences) are:

(a) At ambient pressure the intensity of the triangular plateau maximum decreases by a few per cent from deuterated $(TMTSF)_2PF_6-D_{12}$ to protonated $(TMTSF)_2PF_6-H_{12}$, and

(b) The intensity of the triangular plateau maximum for protonated $(TMTSF)_2PF_6-H_{12}$ decreases from ambient pressure to 7 kbar.

However, Figs. 8 and 9 show that the position of the q_1, q_2 and q_3 singularities do not appreciably shift within $0.01a^*$ and $0.01b^*$. Nevertheless, the intensity of the q_2 singularity for which the response is maximal at 5 K decreases from 2.81 a.u. in $(TMTSF)_2PF_6-D_{12}$

to 2.72 a.u. in $(TMTSF)_2PF_6-H_{12}$ at P_{atm} (i.e.$\sim 3\%$) and then to 2.64 a.u, in $(TMTSF)_2PF_6-H_{12}$ at 7 kbar (i.e. an additional $\sim 3\%$).

5. Discussion

5.1. Shape of the Lindhard function and its relation with the topology of the Fermi surface

The main result of the present work is the first-principles determination of the Lindhard response of the $(TMTSF)_2PF_6$ Bechgaard salt based directly on the real triclinic low-temperature crystal structure. At high temperature (i.e. above ~ 100 K) this function basically exhibits a line maximum at $q_{1D} = 0.5a^*$ (Figs. 4a, 4b and 5a), which corresponds to the $2k_F$ critical wave vector of the 1D band structure, as expected for an electron-hole instability of 1D conductors [16, 26]. However, this line of maxima is found to be slightly modulated in intensity along b^* and exhibits a broad maximum at q_0 (Fig. 5b) which corresponds to the best nesting wave vector of the thermally broadened warped FS (see below). The shape of the Lindhard response changes appreciably below ~ 100 K (Fig. 4) with the onset of a q_2-q_0-q_3 curved arc of maxima, where the a^* component of the q_2 and q_3 singularities differs from $q_{1D} = 0.5a^*$. The intensity of the q_2 and q_3 singularities grows upon cooling (Fig. 7d) and below 20-15 K leads to the appearance of a tilted plateau of maxima with a triangular or, more accurately, a boomerang shape (Fig. 8). A triangular-like maxima of the Lindhard function at 0 K was previously obtained analytically through inclusion of a nesting breaking term t_b' in the quasi-1D electron dispersion built from single sinusoidal intra- (t_a) and inter-chain (t_b) couplings and assuming an *orthorhombic* lattice (when $t_b = 0$ the
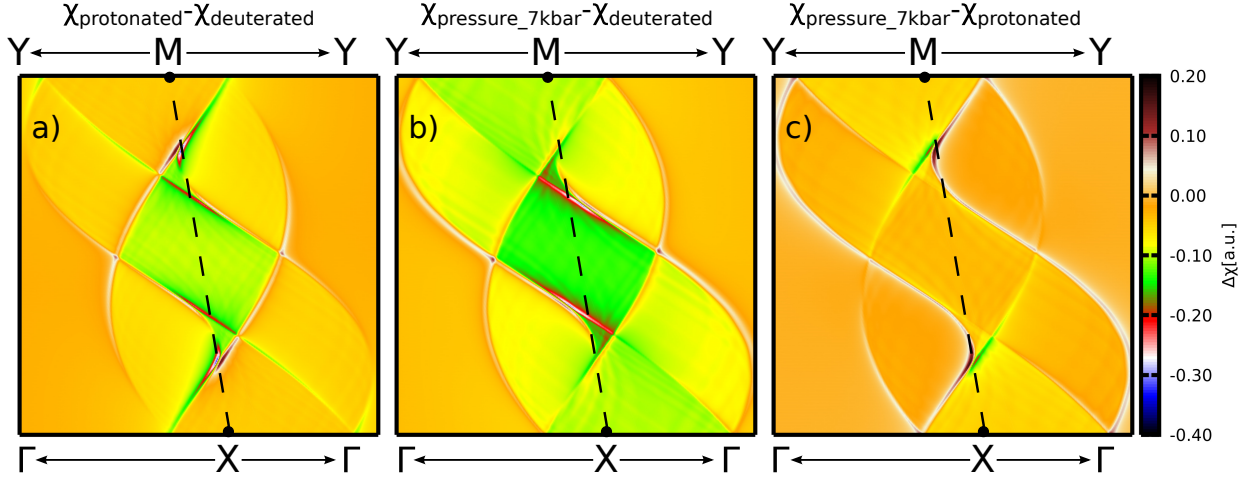
Figure 9. Magnified section of the differences in the Lindhard functions at 5 K between 98% deuterated $(TMTSF)_2PF_6$-D_{12} at P_{atm} and protonated $(TMTSF)_2PF_6$-H_{12} at P_{atm} (a), 98% deuterated $(TMTSF)_2PF_6$-D_{12} at P_{atm} and protonated $(TMTSF)_2PF_6$-H_{12} at 7 kbar pressure (b), protonated $(TMTSF)_2PF_6$-H_{12} at P_{atm} and 7 kbar pressure (c). The X$\rightarrow\Gamma$ and M$\rightarrow$Y arrows are only used to indicate the associate directions. These sections clearly show the sinusoidal singularity lines whose intersection occurs at the q_1, q_2 and q_3 singularity wave vectors.
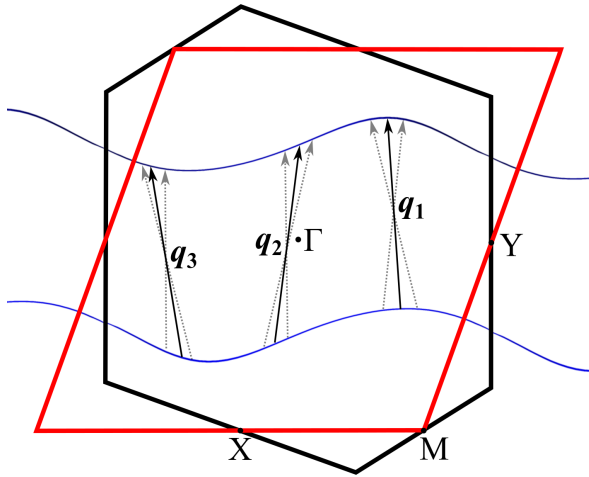

Figure 10. Schematic illustration of the three nesting vectors at the origin of the arcs of the Lindhard function.

Lindhard function diverges at 0 K) [25, 29, 57]. To have the boomerang shape additional inter-chain couplings must be introduced for either the *orthorhomic* [58] and *triclinic* [59] lattices. These calculations also show that the q_0 (which shifts to q_1 upon cooling), q_2 and q_3 singularities are the crossing point of sinusoidal lines of singularities whose analytical expression can be obtained [58, 59]. Such sinusoidal lines of singularities are clearly revealed in our low-temperature calculations (Figs. 4e and Fig. 8) and in the intensity differences of Fig. 9. However, no *ad hoc* FS nesting breaking terms are introduced in the first-principles Lindhard function which only relies on the actual crystal structure of the material.

The progressive growth of a plateau of singularities

in the Lindhard response below 100 K is consistent with the 1D to 2D electronic dimension crossover observed by optics and transport measurements at $T_{CO} \sim 100$ K [6, 13]. In this context the warping of the open FS becomes progressively relevant upon cooling below T_{CO}. In the case of a mainly sinusoidal component of the dispersion of the open FS, the best nesting condition should lead to a main singularity in the Lindhard response. However in our case the best nesting wave vector q_0 is already detected above T_{CO} so that T_{CO} appears to be more likely at the temperature below which two additional nesting wave vectors q_2 and q_3 begin to be detected. Fig. 10 presents the first-principles FS surface of $(TMTSF)_2PF_6$ calculated using the 4 K crystal structure. This figure shows that the warped open FS exhibits three good nesting wave vectors for the q_1, q_2 and q_3 wave vectors which are associated with singularities in the Lindhard function. The occurrence of several FS nesting processes means that the FS has definitely not a regular sinusoidal shape. This is the reason why several additional inter-chain interactions having different k_b dependencies must sizeably contribute to the band dispersion. In other words to account for the first-principles results one must go beyond the *pseudo-orthorhombic* approximation [15, 16] which is based on a sinusoidally shaped FS. This process is carried out in an unbiased way in the DFT calculation.

5.2. Relationship with the $2k_F$ density wave instabilities

The electron-hole Lindhard response of a quasi-1D metal exhibits a maximum for the $2k_F$ chain component wave vector of the associated 1D electron gas. Divergence of this maximum upon cooling is the prerequisite to achieve a $2k_F$ density wave instability. In the presence of a sizeable electron-phonon coupling a $2k_F$ charge density wave (CDW) instability is generated together with, when the phonon field modulates the bond distances, a $2k_F$ bond order wave (BOW) instability. In the presence of exchange interactions due to sizeable on-site electron-electron repulsion, a $2k_F$ SDW instability can occur [15]. Surprisingly, (TMTSF)$_2$PF$_6$ concomitantly exhibits $2k_F$ CDW/BOW and $2k_F$ SDW instabilities at high-temperature.

Weak 1D SDW fluctuations have been detected by NMR below 200 K in (TMTSF)$_2$PF$_6$ [60]. These fluctuations, which are less correlated than those measured in the Fabre salts, grow upon cooling. NMR measurements show also the development of a (3D?) regime of critical fluctuations below $\sim$ 25 K [60, 61]. However, specific heat measurements provide evidence for a very narrow regime of 3D fluctuations starting 0.3 K above T$_{SDW}$= 12 K [62]. Note also that optical measurements provide evidence for the development of a (3D ?) pseudo-gap below 15 K, few K above T$_{SDW}$ [63]. Quasi-1D $2k_F$ BOW fluctuations are detected by X-ray diffuse scattering measurements below about 175 K [64]. In contrast with the SDW fluctuations, the intensity of the $2k_F$ BOW fluctuations saturate below about 100 K (i.e. T$_{CO}$) and vanish below 50 K [20, 55]. This vanishing can be understood as resulting from the increase of the lattice rigidity caused by the strengthening of the linkage of the PF$_6$ anions with the methyl terminal groups of the TMTSF through hydrogen bonding [48].

X-ray diffuse scattering experiments allow to measure the inverse of the correlation length of the BOW fluctuations in the chain direction, ξ_{BOW}^{-1}. The thermal dependence of this quantity is plotted in Fig. 6. This figure clearly shows that ξ_{BOW}^{-1} behaves as the inverse intra-chain electron-hole coherence length of the Lindhard function measured at the q_0 point, $\xi_{eh}^{-1}(q_0)$. This quantitative agreement means that the first-principles Lindhard response brings very relevant information concerning the density wave instability of the Bechgaard salts. Fig. 6 also shows that the inverse electron-hole coherence length $\xi_{eh}^{-1}(q_0)$ decreases weakly upon cooling. It is only below 50 K that the inverse of this quantity exceeds $\lambda_{2k_F} = 2a$ and thus that the $2k_F$ electron-hole modulation wave is spatially defined (above this temperature when $\xi_{eh}(q_0)$ < λ_{2k_F} the electron-hole excitations are thermally

incoherent). An interesting question is to understand why ξ_{eh} remains small for a quite large temperature range. This could be due to the presence of many deviations to a single FS nesting process (Fig. 10).

When the electron-phonon drives the Peierls instability, as found in the blue bronze [65] and in the transition metal trichalcogenides [66], it is possible to observe the critical growth of ξ_{BOW} with respect to a sizeably T dependent ξ_{eh} which exceeds λ_{2k_F} [67] for a large temperature range. The fact that $\xi_{BOW} \approx \xi_{eh}$ in the data of Fig. 6 proves that the electron-phonon coupling is not critical for (TMTSF)$_2$PF$_6$. In contrast, the on-site electron-electron coupling should be critical to achieve the SDW ground state of (TMTSF)$_2$PF$_6$ if one expects a critical growth of ξ_{SDW} over ξ_{eh} for temperatures lower than 50 K. This is apparently what is observed by NMR below $\sim$ 25 K with the critical growth of gaussian fluctuations [61, 60]. Apparently the enhancement of ξ_{SDW} over ξ_{eh} with temperature is small because the SDW pseudo-gap is only detected a few K above T$_{SDW}$ [63].

5.3. Relationship with the $2k_F$ SDW ground state

In the weak coupling limit and random phase approximation (RPA) the maximum of the Lindhard function selects the critical wave vector of the SDW modulation which develops at T$_{SDW}$ [16, 68]. Our first-principles calculation gives a maximum at 12 K for $q_0 = (0.5, 0.23)$, which accounts for the experimental determination. The SDW modulation wave vector has been experimentally determined by fitting the NMR line-shape for (TMTSF)$_2$PF$_6$ assuming that the a^* component of the modulation is $q_{1D}= 2k_F= 0.5$ a^*. Using this assumption it is found that the b^* transverse SDW modulation component lies in the range 0.20 ± 0.05 b^* [21] / 0.24 ± 0.03 b^* [22]. Both determinations correspond, within experimental errors, to the present Lindhard function maximum $q_0= (0.5, 0.23)$ at T$_{SDW}= 12$ K.

However, the first-principles calculation brings more information. In particular, it shows that for temperatures below 20-15 K (i.e. slightly above T$_{SDW}$) the Lindhard response of (TMTSF)$_2$PF$_6$ exhibits a sizable q_2 - q_0 / q_1 - q_3 triangular maximum. Furthermore, the maximum of the response shifts from q_0 to q_1 and then to q_2 around 10 K. This means that within the RPA scenario the SDW modulation wave vector should shift from q_0 to q_1 and then to q_2 when T$_{SDW}$ decreases under pressure. The shift from q_0 to q_1 has been predicted from calculations performed within the *orthorhombic* approximation [16, 25, 29]. Our calculation of the Lindhard response at 5 K for (TMTSF)$_2$PF$_6$ under 7 kbar predicts a q_2 absolute maximum and thus, within the RPA approximation, the stabilization of a q_2 SDW modulation at 7 kbar

(where $T_{SDW} = 4$ K).

In addition, the presence of a wide range of close maxima means that different sets of modulations could be simultaneously (locally) present without any prohibitive cost in magnetic energy. In other words, the SDW ground state could be very fallible, which provides a suitable explanation for the origin of the glassy behavior observed inside the SDW ground state [69]. Along this line it is interesting to remark that the commensurate modulation wave vector $q_c = (1/2, 1/4)$ belongs to the triangular plateau close to the q_1-q_2 singularity line of intensity maximum. Thus the finding in ref. [70] of a local commensurate *lock-in* modulation in the 4 K sub-SDW phase of $(TMTSF)_2PF_6$ can be simply rationalized by the present calculation.

The presence of a triangular q_2 - q_0 / q_1 - q_3 plateau of maxima in the electron-hole response due to a continuous range of FS nesting wave vectors, means that $(TMTSF)_2PF_6$ should be subject to a large panel of 2D magnetic spatial fluctuations. Considering them on the same footing means that one must go beyond a simple RPA approximation of the standard Peierls scenario which selects a single $2k_F$ critical wave vector for which the Lindhard function diverges in order to describe the SDW ground state. In particular a more elaborate mechanism, taking into account the q_2-q_1-q_3 triangular set of fluctuations, could be responsible for the 1st order nature of the SDW transition of $(TMTSF)_2PF_6$ [71], since it has been established that enhanced fluctuations [72, 73] should induce a first order transition.

Another feature which can be discussed in the context of the present calculation concerns the (T,P) SDW phase diagram. In this respect note that (i) $(TMTSF)_2PF_6$-D_{12} is equivalent to the application of a negative pressure of 5 kbar in $(TMTSF)_2PF_6$-H_{12} at P_{atm} [48] and, (ii) there is a strong reduction of T_{SDW} to about 4 K and coexistence between the SDW modulation and superconductivity in $(TMTSF)_2PF_6$-H_{12} at 7 kbar [74]. The finding in our calculations that the q_2 maximum of the Lindhard response at 5 K decreases by 3% from $(TMTSF)_2PF_6$-D_{12} to $(TMTSF)_2PF_6$-H_{12} at $Patm$ and by the same amount in $(TMTSF)_2PF_6$-H_{12} from P_{atm} to 7 kbar shows that within the RPA approximation, the decrease of T_{SDW} under pressure can be simply rationalized by the decrease of the Lindhard response. However at the presence stage of our investigation we cannot still provide a clear-cut explanation of the weak decrease of the Lindhard response because the triangular shaped maxima is not substantially modified from $(TMTSF)_2PF_6$-D_{12} to $(TMTSF)_2PF_6$-H_{12} at 7 kbar (Figs. 8 and 9). This means that nesting breaking effects and additional components to the FS warping

contributing to the triangular shape of the maxima of the Lindhard function [25, 58] do not significantly vary under pressure. Another argument corroborating this finding is that the first-principles calculation leads to the estimation of a quite weak increase of the nesting breaking term t'$_b$ as given by Eq. 2, i. e. from 35.6 meV in $(TMTSF)_2PF_6$-D_{12} to 36.8 meV in $(TMTSF)_2PF_6$-H_{12} at P_{atm} and then to 37.3 meV in $(TMTSF)_2PF_6$-H_{12} at 7kbar. Thus, the present data suggests that the strong reduction of the SDW conductivity gap under pressure [52] should be primarily attributed to the decrease of the optical direct SDW gap related to intra-site Coulomb repulsion more than to the increase of the nesting breaking term t'$_b$, as previously assumed in the literature [15, 16, 53, 25].

6. Concluding remarks

The thermal dependence of the electron-hole Lindhard response of the Bechgaard salt $(TMTSF)_2PF_6$ has been calculated from first-principles using its real triclinic structure. This calculation can be contrasted with earlier calculations based on the *quasi-orthorhombic* approximation of the electronic structure. Contrary to the assumptions in the literature concerning the existence of a single q singularity, our calculation reveals the presence of a low temperature triangular plateau of maxima of the Lindhard response (Fig. 8). This plateau originates from a continuum of FS nesting wave vectors (Fig. 10) which in the first-principles calculation only depend on the details of the low-temperature crystal structure. Indeed our calculation predicts that at P_{atm} the absolute maximum of the response at T_{SDW} accounts for the experimental observation of the q_0 SDW modulation. However the calculation also predicts a shift of the SDW modulation wave vector from q_0 to q_1 and then to q_2. The calculated Lindhard function at 7 kbar shows that the q_2 SDW modulation should be stabilized and thus could coexist with superconductivity instead of q_0-q_1 modulations as previously assumed [74]. The existence of a large plateau of maxima implicates that the $(TMTSF)_2PF_6$ Bechgaard salt is subject to considerable q_2-q_1/q_0-q_3 dependent SDW fluctuations at low-temperature through all the pressure range of the experiments, a feature that was previously ignored in the literature.

Although the mechanism of superconductivity in organic conductors is still the object of a long debate [75], experimental evidence has been accumulated in favor of a pairing mechanism due to incipient SDW fluctuations in the Bechgaard salts [76]. Theoretical analysis has recently pointed out that superconductivity should emerge from an extended quantum critical region of the phase diagram which

is a function of nesting deviation of the FS [77, 78]. In this context the real shape of the electron-hole instability in the P-T region near the superconducting transition T$_S$, together with its relationship with the FS nesting properties, as directly given in the first-principles approach, should be incorporated to improve theoretical treatments.

The modification of the Lindhard response under magnetic field, and the presence of FS breaking effects are important ingredient to calculate a FISDW diagram [16, 57]. The FISDW phase diagram of the literature has been constructed for an *orthorhombic* model taking into account one nesting breaking term t'$_b$. Our results show that one must go beyond this approximation. Only a recent publication builds the FISDW phase diagram by taking into account the various inter-chain interaction of the triclinic lattice [59]. Note that these inter-chain components, which are responsible of subtle modification of the shape of the FS, must be taken into account to explain subtle physical effects such as the sign reversal of the quantum Hall effect [31]. The shape of the FS of the Bechgaard salts also induces a quite large range of additional physical phenomena which can be revealed by the so-called rapid magnetic oscillation phenomena [16]. Such effects have been recently reviewed and analyzed within the *orthorhombic* band dispersion approach for which nesting deviations can be simply modeled [79]. Our study shows that the FS of the real triclinic structure is considerably more complex than that previously considered so that how such effects can modify the present theory of rapid magnetic oscillations is a challenging question.

Although there is no doubt that the model calculations will continue to provide important insights into the remarkable low-temperature physics of the Bechgaard salts, the first-principle approach provides an accurate and unbiased complement to these approaches. It can also take into account in a simple way the 3D effects [56] which are considerably more difficult to model in analytical approaches.

Acknowledments

References

[1] Giamarchi T 2004 *Chem. Rev.* **104** 5037–5056
[2] Thorup N, Rindorf G, Soling H and Bechgaard K 1981 *Acta Crystallogr. B* **37** 1236–1240
[3] Bourbonnais C and Jérome D 2008 Interacting Electrons in Quasi-One-Dimensional Organic Superconductors *The Physics of Organic Superconductors and Conductors* ed Lebed A (Springer, Berlin, Heidelberg) chap 12, p 357–412 ISBN 978-3-540-76667-4
[4] Jacko A C, Feldner H, Rose E, Lissner F, Dressel M, Valenti R and Jeschke H O 2013 *Phys. Rev. B* **87** 155139
[5] Auban-Senzier P, Jérome D, Doiron-Leyraud N, de Cotret S R, Sedeki A, Bourbonnais C, Taillefer L, Alemany P, Canadell E and Bechgaard K 2011 *J. Phys.: Condens. Matter* **23** 345702
[6] Pashkin A, Dressel M, Hanfland M and Kuntscher C A 2010 *Phys. Rev. B* **81** 125109
[7] Jérome D and Schulz H J 1982 *Adv. Phys.* **31** 299–490
[8] Weger M 1978 *J. Phys. Colloques* **39** C6–1456 – C6–1465
[9] Emery V J 1983 *J. Phys. Colloques* **44** C3–977 – C3–982
[10] Bourbonnais C 1985 *Mol. Cryst. Liq. Cryst.* **119** 11–18
[11] Caron L G and Bourbonnais C 1988 *Synth. Met.* **27** A67–A74
[12] Biermann S, Georges A and Lichtenstein A 2001 *Phys. Rev. Lett.* **87** 276405
[13] Moser J, Gabay M, Auban-Senzier P, Jérome D, Bechgaard K and Fabre J M 1998 *Eur. Phys. J. B* **16** 39–46
[14] Coulon C, Delhaes P, Flandrois S, Lagnier R, Bonjour E and Fabre J M 1982 *J. Phys. France* **43** 1059–1067
[15] Yamaji K 1983 *J. Phys. Soc. Jpn.* **51** 2787
[16] Yamaji K, Ishiguro T and Saito G 1998 *Organic Superconductors* (2nd edition, Springer-Verlag, Berlin)
[17] Pouget J P 2015 *Physica B* **460** 45–52
[18] Emery V J, Bruinsma R and Barisic S 1982 *Phys. Rev. Lett.* **48** 1039–1043
[19] Medjanik K, Chernenkaya A, Nepijko S A, Ohrwall G, Foury-Leylekian P, Alemany P, Canadell E, Schonhense G and Pouget J P 2015 *Phys. Chem. Chem. Phys.* **17** 19202–19214
[20] Pouget J P, Alemany P and Canadell E 2018 *Mater. Horiz.* **5** 590–640
[21] Delrieu J M, Roger M, Toffano Z, Moradpour A and Bechgaard K 1986 *J. Phys. France* **47** 839–861
[22] Takahashi T, Maniwa Y, Kawamura H and Saito G 1986 *J. Phys. Soc. Jpn.* **55** 1364–1373
[23] Ducasse L, Abderraba M and Gallois B 1985 *J. Phys. C: Solid State Phys.* **18** L947–L951
[24] Jérome D, Mazaud A, Ribault M and Bechgaard K 1980 *J. Physique Lett.* **41** 95–98
[25] Hasegawa Y and Fukuyama H 1986 *J. Phys. Soc. Jpn.* **55** 3978
[26] Montambaux G 1988 *Phys. Rev. B* **38** 4788–4795
[27] Henderson W, Vescoli V, Tran P, Degiorgi L and Gruner G 1999 *Eur. Phys. J. B* **11** 365–368
[28] Gor'kov L P and Lebed A G 1984 *J. Phys. Lett.* **45** 433–440
[29] Montambaux G, Héritier M and Lederer P 1985 *Phys. Rev. Lett.* **55** 2078–2081
[30] G. Montambaux, Ph. D. Thesis, Université de Paris-Sud (1985).
[31] Zanchi D and Montambaux G 1996 *Phys. Rev. Lett.* **77** 366–369
[32] Alemany P, Pouget J P and Canadell E 2014 *Phys. Rev. B* **89** 155124
[33] Altmeyer M, Valentí R and Jeschke H 2015 *Phys. Rev. B* **91** 245137
[34] Lazić P, Pinterić M, Rivas Góngora D, Pustogow A,

Treptow K, Ivek T, Milat O, Gumhalter B, Doslič N, Dressel M and Tomić 2018 *Phys. Rev. B* **97** 245134

[35] Zhou B, Ishibashi S, Ishii T, Sekine T, Takehara R, Miyagawa K, Kanoda K, Nishibori E and Kobayashi A 2019 *Chem. Comm.* **55** 3327–3330

[36] Hohenberg P and Kohn W 1964 *Phys. Rev.* **136** B864–B871

[37] Kohn W and Sham L J 1965 *Phys. Rev.* **140** A1133–A1138

[38] Soler J M, Artacho E, Gale J D, García A, Junquera J, Ordejón P and Sánchez-Portal D 2002 *J. Phys.: Condens. Matter* **14** 2745–2779

[39] Artacho E, Anglada E, Diéguez O, Gale J D, García A, Junquera J, Martin R M, Ordejón P, Pruneda J M, Sánchez-Portal D and Soler J M 2008 *J. Phys.: Condens. Matter* **20** 064208

[40] Perdew J P, Burke K and Ernzerhof M 1996 *Phys. Rev. Lett.* **77** 3865–3868

[41] Troullier N and Martins J L 1991 *Phys. Rev. B* **43** 1993–2006

[42] Kleinman L and Bylander D M 1982 *Phys. Rev. Lett.* **48** 1425–1428

[43] Louie S G, Froyen S and Cohen M L 1982 *Phys. Rev. B* **26** 1738–1742

[44] Artacho E, Sánchez-Portal D, Ordejón P, García A and Soler J M 1999 *Phys. Stat. Solidi (b)* **215** 809–817

[45] Monkhorst H J and Pack J D 1976 *Phys. Rev. B* **13** 5188–5192

[46] Gallois B, Gaultier J, Hauw C, Lamcharfi T and Filhol A 1986 *Acta Crystallogr. B* **42** 564–575

[47] Gallois B, Gaultier J, Bechtel F, Filhol A and Vettier C 1987 *Mol. Cryst. Liq. Cryst.* **148** 279–293

[48] Foury-Leylekian P, Petit S, Mirebeau I, André G, de Souza M, Lang M, Ressouche E, Moradpour A and Pouget J P 2013 *Phys. Rev. B* **88** 024105

[49] Grant P M 1983 *J. Phys.(Paris)* **44** C3–847 – C3–857

[50] Nakamura K, Nohara Y, Yosimoto Y and Nomura Y 2016 *Phys. Rev. B* **93** 085214

[51] Jacobsen C S, Tanner D B and Bechgaard K 1983 *Phys. Rev. B* **28** 7019–7032

[52] Zámborszky F, Szeghy G, Abdussalam A, Forró L and Mihály G 1999 *Phys. Rev. B* **60** 4414–4417

[53] Degiorgi L, Dressel M, Schwartz A, Alavi B and Grüner C 1996 *Phys. Rev. Lett.* **76** 3838–3841

[54] Pethukov K and Dressel M 2005 *Phys. Rev. B* **71** 073101

[55] Pouget J P 2012 *Crystals* **2** 466–520

[56] B Guster, M Pruneda, P Ordejón, E Canadell, and J-P Pouget 2019 work in progress

[57] Montambaux G 1987 Low dimensional conductors and superconductors *Low Dimensional Conductors and Superconductors* ed Jeróme D and Caron L G (NATO ASI B 155, Plenun Press) p 233–242

[58] Hasegawa Y and Kishigi K 2008 *Phys. Rev. B* **78** 045117

[59] Hasegawa Y and Kishigi K 2010 *Phys. Rev. B* **81** 235118

[60] Wzietek P, Creuzet F, Bourbonnais C, Jérome D, Bechgaard K and Batail P 1993 *J. Phys. I France* **3** 171–201

[61] Creuzet F, Bourbonnais C, Caron L G, Jérome D and Moradpour A 1987 *Synth. Met.* **19** 277–282

[62] Coroneus J, Alavi B and Brown S E 1993 *Phys. Rev. Lett.* **70** 2332–2335

[63] Vescoli V, Degiorgi L, Dressel M, Schwartz A, Henderson W, Alavi B, Gruner G, Brinckmann J and Virosztek A 1999 *Phys. Rev. B* **60** 8019–8027

[64] Pouget J P, Moret R, Comès R, Bechgaard K, Fabre J M and Giral L 1982 *Mol. Cryst. Liq. Cryst.* **79** 485–499

[65] Guster B, Pruneda M, Ordejón P, Canadell E and Pouget J P 2019 *Phys. Rev. Mater.* **3** 055001

[66] B Guster and M Pruneda and P Ordejón and E Canadell and J-P Pouget 2019 Phys. Rev. Mater. submitted for publication

[67] Pouget J P 2016 *C. R. Phys.* **17** 332–356

[68] Grüner G 1994 *Rev. Mod. Phys.* **60** 1–24

[69] Monceau P 2012 *Adv. Phys.* **61** 325–581

[70] Nagata S, Misawa M, Ihara Y and Kawamoto A 2013 *Phys. Rev. Lett.* **110** 167001

[71] Clark W G, Hanson M E, Wong W H and Alavi B 1994 *Physica B* **194–196** 285–286

[72] Bak P 1980 Theory of elastic phase transitions and soft acoustic modes *Modern Trends in the Theory of Condensed Matter* ed Pekalski A and Przystawa J A (Lecture Notes in Physics vol. 115, Springer-Verlag, Berlin Heidelberg) p 414–431

[73] More explicitly, if for simplicity one only considers fluctuations associated to the nearly equal maxima q_0 and q_1 of the Lindhard function at T_{SDW} for $(TMTSF)_2PF_6$, the free energy Landau development associated to the complex order parameters η_1 and η_2, corresponding to the q_0 and q_1 modulations, respectively, can be schematically written as $F = a_1 \mid \eta_1 \mid^2 + a_2 \mid \eta_2 \mid^2 + u_1 \mid \eta_1 \mid^4 + u_2 \mid \eta_2 \mid^4 + w \mid \eta_1 \mid^2 \mid \eta_2 \mid^2$. The treatment of F using renormalization group methods lead to a regime where the fourth order terms are no longer positive definite, which conducts to a first order transition.

[74] Vuletic T, Auban-Senzier P, Pasquier C, Tomic S, Jérome D, Héritier M and Bechgaard K 2002 *Eur. Phys. J. B* **25** 319–331

[75] Ardavan A, Brown S, Kagoshima S, Kanoda K, Kuroki M, Mori H, Ogata M, Uji S and Wosnitza J 2012 *J. Phys. Soc. Jpn.* **81** 011004

[76] Jérome D and Yonezawa S 2016 *C. R. Physique* **17** 357–375

[77] Sedeki A, Bergeron D and Bourbonnais C 2012 *Phys. Rev. B* **85** 165129

[78] Shahbazi M and Bourbonnais C 2016 *Phys. Rev. B* **94** 195153

[79] Montambaux G and Jérome D 2016 *C. R. Physique* **17** 376–388